



1 **Aerodynamic size-resolved composition and cloud**
2 **condensation nuclei properties of aerosols in Beijing**
3 **suburban region**
4

5 Chenjie Yu^{1,2}, Dantong Liu¹, Kang Hu¹, Ping Tian³, Yangzhou Wu¹, Delong Zhao³,
6 Huihui Wu², Dawei Hu², Wenbo Guo², Qiang Li⁴, Mengyu Huang³, Deping Ding³ and
7 James D. Allan^{2,5}

8

9 ¹Department of Atmospheric Sciences, School of Earth Sciences, Zhejiang University, Zhejiang 310027,
10 China

11 ²Department of Earth and Environmental Sciences, University of Manchester, Manchester M13 9PL,
12 United Kingdom

13 ³Beijing Weather Modification Office, Beijing 100089, China

14 ⁴Cambustion Ltd China Office, Shanghai 201112, China

15 ⁵National Centre for Atmospheric Sciences, University of Manchester, Manchester M13 9PL, United
16 Kingdom

17 *Correspondence to: Dantong Liu (dantongliu@zju.edu.cn) and James Allan*
18 *(james.allan@manchester.ac.uk)*

19

20

21

22

23

24

25

26

27



28 **Abstract** The size-resolved physiochemical properties of aerosols determine their
29 atmospheric lifetime, cloud interactions, and the deposition rate on human respiratory
30 system, however most atmospheric composition studies tend to evaluate these
31 properties in bulk. This study investigated size-resolved constituents of aerosols on
32 mass and number basis, and their droplet activation properties, by coupling a suite of
33 online measurements with an aerosol aerodynamic classifier (AAC) based on
34 aerodynamic diameter (D_a) in Pinggu, a suburb of Beijing. While organic matter
35 accounted for a large fraction of mass, a higher contribution of particulate nitrate at
36 larger sizes ($D_a > 300$ nm) was found under polluted cases. By applying the mixing
37 state of refractory black carbon containing particles (rBCc) and composition-dependent
38 densities, aerosols including rBCc were confirmed nearly spherical at $D_a > 300$ nm.
39 Importantly, the number fraction of rBCc was found to increase with D_a at all pollution
40 levels. The number fraction of rBC is found to increase from ~3% at ~90 nm to ~15%
41 at ~1000 nm, and this increasing rBC number fraction may be caused by the coagulation
42 during atmospheric aging. The droplet activation diameter at a water supersaturation of
43 0.2% was 112 ± 6 nm and 193 ± 41 nm for all particles with D_a smaller than $1 \mu\text{m}$
44 (PM_{10}) and rBCc respectively. As high as $52 \pm 6\%$ of rBCc and $50 \pm 4\%$ of all PM_{10}
45 particles in number could be activated under heavy pollution due to enlarged particle
46 size, which could be predicted by applying the volume-mixing of substance
47 hygroscopicity within rBCc. As rBCc contributes to the quantity of aerosols at larger
48 particle size, these thickly coated rBC may contribute to the radiation absorption
49 significantly or act as an important source of cloud condensation nuclei (CCN). This
50 size regime may also exert important health effects due to their higher deposition rate.

51

52 1. Introduction

53 Atmospheric aerosols make a significant contribution in a number of atmospheric
54 chemical and physical processes (Riemer et al., 2019). Aerosols from anthropogenic
55 emissions have negative impact on air quality and human health (West et al., 2016). As
56 a major megacity, the air pollution in Beijing and its surrounding regions has raised
57 much attention in the past years (Shi et al., 2019). The rapid urbanization and the
58 continued increase in vehicle numbers have contributed to a complicated air pollution



59 situation in Beijing (Squires et al., 2020). A number of in-situ measurements have
60 characterised the submicron aerosol compositions in urban Beijing (Wang et al.,
61 2020;Hu et al., 2016;Wang et al., 2019). However, few studies have detailed
62 characterised the fine particle compositions or cloud condensation nuclei (CCN)
63 abilities at Beijing rural sites (Chen et al., 2020a). The relocation of industry from the
64 urban Beijing has led the surrounding cities around Beijing to be highly industrialised
65 in recent years (Wang et al., 2018), and the rural sites of Beijing are significantly
66 impacted by the air pollutants transported from the surrounding industrial regions in
67 North China Plain (NCP) (Wu et al., 2011). Furthermore, controls targeting pollution
68 from residential solid fuel use and diesel vehicles do not apply outside of the main
69 metropolitan area of Beijing. Detailed characterisation of fine aerosol physiochemical
70 properties in a variety of different environments is essential to understand the evolution
71 of atmospheric particulate matter.

72

73 Fine particulate matter can also cause damage to human respiratory system (Xing et al.,
74 2016;Xu et al., 2016). Aerodynamic size of aerosols crucially determines their
75 deposition to the respiratory system (Sturm, 2010;Vu et al., 2018;Sturm, 2017), e.g.
76 particle with aerodynamic diameter (D_a) below 2.5 μm can reach small air ways of
77 respiratory system and further pass into the blood (Lipworth et al., 2014). The observed
78 toxicity of aerosols is composition dependent (Kwon et al., 2020) and influenced by the
79 complex morphology (Sturm, 2010;Vu et al., 2018), therefore the aerodynamic size-
80 resolved properties of aerosols are important to understand their influences on air
81 quality associated with the human health.

82

83 Atmospheric aerosols also play important roles in climate through scattering and
84 absorbing solar radiation directly, or indirectly through altering cloud properties (Liu
85 et al., 2020;Ravishankara et al., 2015). Black carbon (BC) is produced from incomplete
86 combustion and is the dominant optically absorbing component in aerosols (Liu et al.,
87 2020;Bond et al., 2013). By mixing with other compounds, the absorption ability of
88 coated BC can be enhanced through the “lensing effect” (Lack and Cappa, 2010).
89 However, detailed simulation and characterization of optical properties of BC remains



90 large uncertain since it is influenced by factors such as shape and mixing state (Cappa
91 et al., 2012;Liu et al., 2017;Fierce et al., 2020), which can be modified through
92 atmospheric processing. Thus, better characterization of light absorbing carbonaceous
93 particles is essential.

94

95 Coated BC is also known as an important source of CCN and wet removal is its main
96 atmospheric loss mechanism, so its in-cloud scavenging efficiency and thus lifetime is
97 influenced by its size, mixing state and hygroscopic properties (Taylor et al., 2014), but
98 this is subject to large uncertainties (Myhre and Samset, 2015). Studies have confirmed
99 that hygroscopicity of rBCc is largely impacted by the coating material, and rBCc will
100 transform from hydrophobic to hydrophilic after emission by acquiring more non-BC
101 material and increasing in size (Hu et al., 2020b;Wu et al., 2019;Liu et al., 2013).
102 However, limited studies (Levin et al., 2014;Broekhuizen et al., 2006) have provided
103 both the measured size-resolved CCN ability and aerosol physiochemical properties so
104 far, and the CCN ability of rBCc based on atmospheric data remains poorly constrained.
105 Previously, size-resolved composition has been widely investigated using size-
106 segregated off-line analysis of cascade impactors samples (Marple et al., 1991). This
107 technique offers great advantages in obtaining detailed information about compositions
108 in combination of the advanced offline measurements, however it often requires large
109 amounts of material and may not be able to provide sufficient time resolutions.
110 Information about particle mixing state and CCN activities are also not available
111 through this technique. The aerosol mass spectrometer (AMS) is also capable of
112 delivering size-resolved aerosol compositions, however the poor accuracy of AMS in
113 the size range important for CCN (typically 50 -100 nm) has hampered quantitative
114 work for this application.

115

116 A previous study (Yu et al., 2020) has characterized the size-resolved rBCc mixing
117 state in Beijing using a tandem aerosol classifier system. To explore the size-resolved
118 physiochemical properties and CCN ability for bulk aerosol compositions, here we
119 performed a new online measurement method by coupling an aerodynamic aerosol



120 classifier (AAC) with different aerosol measurement techniques including a single-
121 particle soot photometer (SP2) and an aerosol mass spectrometer (AMS). Comparing
122 to the previous studies performed with differential mobility analyzer (DMA), the AAC
123 classifies particles without multiple charging artefacts in a wide size range and with
124 better transmission efficiency (Johnson et al., 2018). The simultaneous measurement of
125 size-resolved chemical composition and CCN activation enables a detailed analysis of
126 rBCc hygroscopicity and its size-dependent contribution to the CCN activation in a
127 polluted environment. This information will deliver a better understanding to the BC
128 deposition properties for the climate and air pollution impact on human health studies.

129

130 **2. Experimental methods**

131 **2.1 Experiment location and instruments**

132 The experiment was performed between 5th Jan and 20th Jan 2020 in the Beijing
133 Weather Modification Office field experiment base located in Pinggu (the red
134 pentagram shown in Fig. 4a), a northeastern suburb of Beijing (Shi et al., 2019). With
135 agriculture dominated its local economy, Pinggu is surrounded by small villages and
136 farmlands (Han et al., 2020). Fig. 1 describes the schematic of the instruments used for
137 the size-resolved aerosol measurements. An aerodynamic aerosol classifier (AAC,
138 Cambustion) was placed upstream of the aerosol measurement instruments. The
139 operation and validation of the AAC was described in previous studies (Tavakoli and
140 Olfert, 2013; Tavakoli and Olfert, 2014). Unlike the DMA or Centrifugal Particle Mass
141 Analyzer (CPMA), the AAC selects particles based on aerodynamic sizes according to
142 particle relaxation time without needing charging for electrostatic or mass sizing. A
143 suite of online measurements was introduced downstream of the AAC, including a
144 high-resolution time of flight aerosol mass spectrometer (HR-ToF-AMS, Aerodyne)
145 (DeCarlo et al., 2006) was operated in V-mode to characterize the non-refractory
146 aerosol composition and a single particle soot photometer (SP2, DMT) (Schwarz et al.,
147 2010) for the measurement of rBCc concentrations. The volume properties of non-
148 refractory material within rBCc (hence referred as ‘coating thickness’) was derived by
149 SP2 leading-edge-only (LEO) method (Liu et al., 2019) and is described as the ratio
150 between the diameter of total rBCc and rBC core (D_p/D_c). A cloud condensation nuclei



151 counter (CCNc, DMT) was used to sample the potential CCN activation ability at a
152 constant supersaturation (SS) of 0.2% and a condensation particle counter (CPC, TSI
153 model 3776) was used to measure the condensation nuclei (CN) number concentration.
154 The SP2 incandescence signal was calibrated using nebulised Aquadag black carbon
155 particle standards while the scattering channel was calibrated by 200 nm polystyrene
156 latex spheres before the measurement, and the correction factor of 0.75 for ambient rBC
157 measurement was applied (Laborde et al., 2012). The ionization efficiency of AMS was
158 calibrated using mono-disperse of nebulized ammonium nitrate particles following the
159 standard protocols (Xu et al., 2017), and a constant collection efficiency (CE) of 0.5 is
160 applied (Middlebrook et al., 2012). More details of the calibration and operation of this
161 AMS instrument can be seen in previous field measurement studies (Hu et al., 2021; Liu
162 et al., 2021). The term ‘all particles’ in this study is referred as the PM₁ compositions
163 including Organic compounds (Org), Sulfate (SO₄), ammonia (NH₄), Nitrate (NO₃),
164 Chloride (Cl) and rBC from AMS and SP2. The AAC was set to classify dry aerosol
165 particles from 90 nm to 1100 nm in aerodynamic diameter (D_a) to cover the detection
166 range of the SP2 and AMS. It took around 15 min to complete one scan using the AAC
167 step scanning mode, and a timed valve was placed at the upstream of the AAC for
168 switching between monodisperse and polydisperse every 30 min. Example for a
169 running cycle is presented in the supplementary.

170

171 2.2 Calculation of aerosol morphology parameters

172 The dynamic shape factor (χ) describes the shape of particles (DeCarlo et al., 2004).
173 $\chi = 1$ denotes a perfectly spherical particle, and $\chi > 1$ means more non-sphericity.
174 Based on the measurement here, χ can be calculated by:

$$175 \quad \chi = \frac{\rho_p D_v^2 C_c(D_v)}{D_a^2 C_c(D_a)} \quad (1)$$

176 where ρ_p is the particle material density, C_c represents the slip correction factor at a
177 given diameter and is calculated following the description in Kim et al. (2005), D_v is
178 the particle volume equivalent diameter, and D_a is the aerodynamic diameter classified
179 by AAC. This calculation is performed for all particles (including rBCc) and rBCc,
180 using their respective parameters (ρ_p and D_v). For all particles, ρ_p is the mean density
181 weighted by the PM₁ results measured by the AMS and SP2. To compute the particle
182 volume results based on the AMS measured ion and Org concentrations, a simplified



183 ion pairing scheme presented in Gysel et al. (2007) was applied, and the solutions are
184 described in the supplementary. The ρ_p of rBCc is calculated as the weighted density
185 within rBCc including rBC and coatings, where the coating material of rBCc is assumed
186 to constitute of the same volume fractions of ambient non-refractory compositions (Liu
187 et al., 2015;Hu et al., 2021):

$$188 \quad \rho_{\text{rBCc}} = \frac{M_{\text{rBCc}}}{V_{\text{rBCc}}} = \frac{\rho_{\text{NR}} \cdot \left(\frac{1}{6} \pi D_{\text{p,rBCc}}^3 - \frac{1}{6} \pi D_c^3 \right) + M_{\text{rBC}}}{\frac{1}{6} \pi D_{\text{p,rBCc}}^3} \quad (2)$$

189 where M_{rBCc} and V_{rBCc} are the mass and volume of the rBCc respectively, ρ_{NR} is the
190 particle density of non-refractory compositions. The rBC core diameter (D_c) and total
191 rBCc diameter ($D_{\text{p,rBCc}}$) are derived through the SP2 LEO method.

192 For all particles, mean single particle mass is derived from the total mass (M_{all})
193 obtained by AMS and SP2 divided by the total number (N_{total}) obtained by the CPC,
194 hereinafter the mean D_v of particle is assumed to equal to the mass equivalent diameter
195 (D_m) and is obtained by applying the mean ρ_p above:

$$196 \quad D_{v,\text{all}} = D_{m,\text{all}} = \sqrt[3]{\frac{6M_{\text{single,all}}}{\rho_{\text{all}} \cdot \pi}} = \sqrt[3]{\frac{6M_{\text{all}}}{\rho_{\text{all}} \cdot \pi \cdot N_{\text{total}}}} \quad (3)$$

197 where ρ_{all} is the particle density of all aerosol particles.

198

199 **2.3 Hygroscopicity parameter calculation**

200 The hygroscopicity parameter (κ) (Petters and Kreidenweis, 2007) of measured
201 aerosols is predicted based on the measured aerosol compositions and invoking the
202 Zdanovskii–Stokes–Robinson (ZSR) mixing rule(Stokes and Robinson, 1966). The κ
203 for all particles (κ_{all}) is calculated as:

$$204 \quad \kappa_{\text{all}} = \sum_i \varepsilon_i \kappa_i \quad (4)$$

205 where ε_i and κ_i is the volume fraction and hygroscopicity parameter of each chemical
206 composition respectively. The κ based on the AMS measured concentrations were
207 calculated based on the same simplified ion pairing scheme described above. The
208 detailed information for each parameter used for κ calculation is listed in Table S1. For
209 rBCc, the κ_{rBCc} is calculated by:

$$210 \quad \kappa_{\text{rBCc}} = \sum_i \varepsilon_{\text{coating},i} \kappa_{\text{coating},i} + \varepsilon_{\text{rBC}} \kappa_{\text{rBC}} \quad (5)$$



211 Where $\varepsilon_{\text{coating},i}$ and ε_{rBC} is the volume fraction coating and rBC respectively; $\kappa_{\text{coating},i}$
212 represents the hygroscopicity parameter for each rBCc coating composition and is
213 assumed to equal to the κ of ambient non-refractory compositions (Motos et al.,
214 2019;Hu et al., 2021); κ_{rBC} represents the hygroscopicity parameter for rBC and the
215 last term can be ignored since pure rBC is assumed to be hydrophobic.

216

217 **2.4 CCN ability of all particles and rBCc**

218 The CCN activation fraction is determined as the ratio between CCN number
219 concentration at SS=0.2% and the CN number concentration measured by the CPC. The
220 size-resolved CCN activation fraction (AF) is fitted in a sigmoid function:

$$221 \quad AF = \frac{E}{1 + \left(\frac{D_{50}}{D_p}\right)^C} \times 100\% \quad (6)$$

222 Where E and C are fitting coefficients which represent the asymptote and the slope
223 respectively. D_p is the particle dry diameter, and D_{50} represents the critical particle
224 diameter where 50% of particles in number can be activated as CCN (Petters and
225 Kreidenweis, 2007).

226

227 The number concentration of rBCc which acts as CCN is derived from the concurrent
228 measurements of rBC number concentration, CCN and CN. The method described by
229 Hu et al. (2021) has been applied to determine the activation of rBCc. Firstly, the un-
230 activated particle number concentration is derived from the difference between CN and
231 CCN, as the red line in Fig. 2(a) shows. For particles with $D_a > 300\text{nm}$ in the example,
232 the un-activated particles are nil thus all rBCc is also activated. Here particles are
233 considered to be well mixed, and rBCc is less hydrophilic than any other non-refractory
234 particles at the same particle size. Thus, the rBCc is more difficult to be activated as
235 CCN than the other particles. For particles with $D_a < 300\text{nm}$, the rBCc is therefore
236 considered to be the first in contributing the un-activated particles and the activated
237 rBCc is the rBCc number concentration higher than the un-activated particle numbers.
238 By this way, the size-dependent activated rBCc number concentration can be obtained
239 (black line in Fig. 2(b)). $D_{50, \text{rBCc}}$ can then be derived through Equation (6) based on the
240 rBCc activation fraction curve. The rBCc activation fraction derived through this
241 method is further referred as “measured AF_{rBCc} ”. There may be some occasions when
242 rBCc could exhibit a higher hygroscopicity, if coated with sufficient hygroscopic



243 substances, even higher than a particle without containing rBC. This means the scenario
244 here may underestimate some fractions of activated rBCc. The method here may
245 therefore serve as a least estimation of droplet activation of rBCc from this aspect.

246

247 The rBCc activation is also estimated through the calculated size-resolved critical
248 supersaturation (SS_c) (Wu et al., 2019; Hu et al., 2021) for comparison, which is derived
249 based on the κ_{rBCc} described before from the κ -Köhler theory:

$$250 \quad S(D) = \frac{D^3 - D_{rBCc}^3}{D^3 - D_{rBCc}^3(1 - \kappa)} \exp\left(\frac{4\sigma_{s/a}M_w}{RT\rho_w D}\right) \quad (7)$$

251 Where D is the diameter of the droplet, D_{rBCc} is the rBCc dry diameter, M_w and ρ_w are
252 the molecular weight and density of water respectively, T is temperature, R is the idea
253 gas constant, and $\sigma_{s/a}$ is the surface tension of the solution/air interface. A decreased
254 SS with increasing D_a can be obtained (Fig. 3), so the $D_{50, rBCc}$ at $SS_c = 0.2\%$ is the cross
255 point above which diameter only $SS < 0.2\%$ is required to activate the targeting rBCc.
256 The activated rBCc number concentration is the rBCc concentration with size larger
257 than $D_{50, rBCc}$. The activation fraction estimated through this method is further referred
258 as “modelled AF_{rBCc} ”.

259

260 **2.5 NAME dispersion model**

261 The air mass classification results used to identify potential source regions are generated
262 by the UK Met Office Numerical Atmospheric dispersion Modelling Environment
263 (NAME) dispersion model (Jones et al., 2007). The model presented the 48h backward
264 dispersion results on a $0.25^\circ \times 0.25^\circ$ grid using the three-dimensional gridded
265 meteorological field generated from the UK Met Office’s Unified Model (Brown et al.,
266 2012). Beijing and its surrounding areas have been classified into five regions as shown
267 in Fig. 4(a) in order to attribute the air mass histories: The Local Beijing (39-41.5°N,
268 115-117°E), the North (41.5-45°N, 104-121°E), the South (32-39°N, 115-121°E), the
269 West (32-41.5°N, 104-115°E) and the East region (39-41.5°N, 117-121°E).

270

271 **3. Results and discussions**

272 **3.1 Overview for the whole campaign period**

273 Fig. 4(c) presents the overview of aerosol total number and mass concentrations during
274 the experimental period. Beijing and its suburban region experience large contrasts in



275 pollution conditions depending on the wind direction (Liu et al., 2019;Chen et al.,
276 2020b). To test whether the mixing state varies according to ambient pollution
277 concentrations, the pollution is classified into three levels according to the frequency
278 distribution of PM_{10} concentrations during the whole measurement period: heavy
279 pollution ($PM_{10} \geq 30 \mu\text{g}/\text{m}^3$), moderate pollution ($10 \mu\text{g}/\text{m}^3 < PM_{10} < 30 \mu\text{g}/\text{m}^3$), and
280 light pollution ($PM_{10} \leq 10 \mu\text{g}/\text{m}^3$). Combining the airmass history results with the
281 aerosol optical depth (AOD) spatial distribution results from the Himawari-8 Level 2
282 aerosol product (Bessho et al., 2016;Fukuda et al., 2013) (Fig. 4(b)), the heavy and
283 moderate pollution period was mostly attributed to airmasses from the East and West
284 regions. While the contribution from the Local airmass cannot be ignored in some
285 pollution cases, relatively clean northerly airmasses were associated with the light
286 pollution periods.

287

288 **3.2 Size-resolved aerosol mass compositions and rBCc mixing state**

289 Fig. 5(a-e) presents the size-resolved average mass concentrations for PM_{10} , rBC,
290 organic compounds (Org), sulfate (SO_4), nitrate (NO_3) respectively under each
291 pollution condition. Though the heavy pollution period has the highest aerosol mass
292 concentrations among three cases, there was no significant difference for total PM_{10} and
293 non-refractory compositions mass concentrations below 200 nm in D_a under different
294 pollution levels. Notable contributions to the total PM_{10} from non-refractory material
295 was observed for $D_a > 300$ nm especially for the heavy pollution condition. Unlike the
296 more polluted conditions, the non-refractory aerosol mass concentrations during light
297 pollution periods shows limited size-dependent variation. The size distribution of rBC
298 mass concentration reached the peak at 400 nm under heavy pollution, while the peak
299 for the moderate and light pollution was at a bit smaller D_a which was between 300 and
300 400 nm. The peak diameter of NR- PM_{10} observed in Pinggu was at around 700 nm and
301 is higher than the peak diameter of NR- PM_{10} reported at the urban site of Beijing which
302 is between 400 nm and 500 nm in winter (Hu et al., 2016). Due to the higher primary
303 organic aerosol (POA) emissions, the results at Beijing urban site has higher
304 contribution of Org at smaller size (< 500 nm) (Zhang et al., 2014). While the higher
305 Org peak diameter (at around 700 nm) shown in our study suggests that the Org was
306 highly oxidised in Beijing suburban (Li et al., 2021). The higher peak diameter of
307 secondary inorganic compound also indicates the well mixture of aerosol components



308 in suburban region (Liu et al., 2016). This size-resolved composition result reported in
309 Pinggu is in consistent with the previous measurement in another suburban region in
310 NCP (Li et al., 2021). Comparing the composition mass fractions under three different
311 pollution cases shown in Fig.5(i-k), one of the remarkable differences is that particulate
312 nitrate accounted more mass fraction during the heavy and moderate pollution periods
313 than during the light pollution period. Previous studies shown that this rapid particulate
314 nitrate formation in Beijing area is mainly associated with the heterogeneous hydrolysis
315 of N_2O_5 at night (Li et al., 2018). Particulate nitrate has become one of the major
316 secondary inorganic aerosol pollutants in urban environment recently (Zhang et al.,
317 2015), and NO_3 also contributed to the aerosol hygroscopicity significantly during the
318 haze pollution periods (Sun et al., 2018). Due to the significant reduction of SO_x
319 emissions in China in recent years (Zhang et al., 2012), the mass fractions of SO_4
320 remained low in pollution cases. The Org contributed to the aerosol mass compositions
321 significantly, and the capping of rBC mass fraction was around 25% among all three
322 cases.

323

324 Fig. 5(f) and (g) present the size distribution of rBC core mass median diameter (MMD)
325 and the coating thickness. This indicates larger D_a had selected rBCc with larger rBC
326 core and higher coatings. The MMD of rBC core increased from below 100 nm to
327 around 300 nm with the increasing of particle size. The rBC core for the light pollution
328 condition was a little smaller than the other two periods, indicating a possible
329 coagulation process in more polluted cases with higher rBC concentrations. The coating
330 thickness of rBCc D_p/D_c decreased slightly when D_a increased from 90 to 300 nm. This
331 decreasing trend of rBC coating thickness may be caused by the traffic emissions. Joshi
332 et al. (2021) demonstrated that traffic emissions dominated the rBC fluxes in urban
333 Beijing, and a previous study also showed a similar decreasing trend of rBC coatings
334 for engine emissions within this particle size range (Han et al., 2019). Limited
335 differences were observed for the size-resolved D_p/D_c among the three pollution levels.
336 The average D_p/D_c for all rBCc was 2.1 ± 0.2 , 1.6 ± 0.1 , and 1.5 ± 0.04 for heavy,
337 moderate and light pollution respectively. There was more heavily coated rBCc showed
338 for heavy pollution condition, and this was consistent with more secondary particle
339 formation than the other periods.

340



341 Fig. 5(h) shows the distribution of hygroscopicity parameter (κ). The lowest κ_{all}
342 between 150 and 300 nm at heavy and moderate pollution condition was mainly caused
343 by the increasing of rBC fractions. Due to the increase of more hydroscopic inorganic
344 compositions for larger particles under heavy and moderate pollution conditions, κ_{all}
345 increased considerably for particles $D_a > 200$ nm and 300 nm. In contrast to the more
346 polluted cases, κ_{all} under light pollution period varied slightly with the increase of D_a .
347 Caused by the absence of more soluble inorganic compositions, κ_{all} for particles with
348 $D_a > 300$ nm during light pollution period was lower than the other conditions. For
349 rBCc, κ_{rBCc} was more influenced by the coating volume fractions rather than the
350 coating compositions, as the variation of κ_{rBCc} generally followed the trend of rBCc
351 coating thickness (Fig. 5(g)). κ_{rBCc} for particles with $D_a < 300$ nm was close under three
352 different pollution levels, and the decreasing trend of κ_{rBCc} between 90 and 300 nm
353 was caused by the reduction of coating material fraction.

354

355 3.3 Size-resolved particle morphology

356 Fig. 6 shows the distribution of particle density, average single particle size and mass,
357 and morphology parameters for all particles (left) and rBCc (right). The average particle
358 density for all particles (ρ_{all}) varied slightly between 1.55 and 1.6 g/cm³, and the rBCc
359 particle density (ρ_{rBCc}) within the measurement size range was generally higher than
360 the ρ_{all} due to the higher density of rBC. The peak ρ_{rBCc} reached at between 200 and
361 300 nm in D_a due to the rBCc was least coated within this size range. D_v was larger
362 than D_a and deviated more at smaller size but was close to D_a for all particles and rBCc
363 larger than 200 nm. The dynamic shape factor (χ) of all particles declined from around
364 1.8 to 1.2, while χ of rBCc declined from around 2 to 1.2. All particles with D_a above
365 400 nm and rBCc with D_a above 500 nm tended to have lower χ which was around 1.2.
366 Previous study (Lin et al., 2015) in other megacities reported that χ of all particles was
367 around 2 with D_a at around 100 nm which is close to our results. Previous measurements
368 (Zhang et al., 2016) in Beijing also shown the similar decreasing trend of χ for rBC
369 core during the aging process.

370

371 This result indicates that smaller particles have more irregular shapes, while particles
372 with larger aerodynamic size are more spherical in ambient atmosphere. Previous
373 experiment shows that the irregular aggregated rBCc from fresh emissions can



374 transform to be more spherical-like by acquiring more secondary species(Ahern et al.,
375 2016). Our results confirm that the spherical assumption is suitable for large rBCc in
376 aerodynamic size in a typical anthropogenic polluted environment. This also implies
377 that larger and spherical particles tend to have larger deposition rate, while particles
378 with more irregularity may experience higher drag force in the air, towards decelerating
379 the settlement.

380

381 **3.4 Size-resolved CN and CCN number concentrations**

382 Fig.7(a) and (b) presents the distribution of rBCc, CN and CCN number concentrations
383 at different polluted conditions. The peak of rBCc number concentration at heavy
384 pollution period was at around 300 nm, while the peak for moderate and light pollution
385 was slightly smaller (at around 200 nm). This agrees with the previous studies in Beijing
386 showing that the average total rBCc particles size was associated with the pollution
387 levels (Yu et al., 2020;Liu et al., 2019). Similar trend was also observed for the CN
388 concentrations, and the peak of CN concentrations shifted to the larger particle size with
389 increased pollution level. Higher levels of secondary production through condensation
390 and also coagulation enlarged particle size. Because of the increasing of average
391 particle size, more fraction of particles can be activated as CCN under heavy pollution
392 period.

393

394 By using aerodynamic size-resolved number concentration of rBC and CN, a
395 remarkable increase of rBC number fraction at larger aerodynamic size was found (Fig
396 7(c)), i.e. with D_a from 100-1000nm, rBC number fraction increased almost linearly
397 from 3% to 15%, and this applied to all pollution levels. This tends to represent a
398 generic phenomenon for a suburban environment with continuous influence of
399 anthropogenic emissions, and the primary emissions had been aged in a time scale of
400 hours. Fine rBC condensed on or coagulated with pre-existing larger particles during
401 the aging process (Riemer et al., 2009). The coagulation process dominated the
402 formation of thickly-coated rBC particles (Reddington et al., 2013), and the coagulation
403 rate of smaller rBC may be fast due to the higher number concentration of fine mode
404 particles (Matsui et al., 2018). The very fresh emissions such as from diesel engine
405 emissions, which mostly contains thinly-coated small rBC (Han et al., 2019), may not
406 show the same rBC number fraction distribution. Previous studies also reported a



407 relatively fast aging process for BC also in the order of hours (Peng et al., 2017), if
408 under a polluted environment rich of precursors, the aging could be even faster (Peng
409 et al., 2016). The causality of this increased rBC number fraction at larger particle size
410 is therefore the non-rBC compounds associated with it. The results presented here
411 indicated that the higher contribution from regional pollution to the rBC number at
412 larger aerodynamic size may apply, albeit the various features of primary sources in
413 winter (Wang et al., 2019;Liu et al., 2019).

414

415 The rBC associated with larger coatings was more spherical (with χ close to 1, as
416 discussed above), therefore more likely to have a core-shell structure, which would lead
417 to an absorption enhancement from the lensing effect of coatings (Liu et al., 2017). In
418 addition, this size-resolved rBC number fraction results will improve the understanding
419 to the lung deposition of BC in human health studies (Rissler et al., 2017). This means
420 for particles with higher deposition rate tend to contain a higher number fraction of
421 rBC, which may provide some indications for constituents deposited on different parts
422 in human respiratory system (Carvalho et al., 2011;Manigrasso et al., 2020).

423

424

425 **3.5 CCN ability and rBCc activation**

426 Presented in Fig. 8(a), the $D_{50, All}$ varied smoothly and was slightly higher than 100 nm
427 for most of the experiment period. The mean $D_{50, All}$ and $D_{50, rBCc}$ was 112 ± 6 nm and
428 193 ± 41 nm respectively. Shown in Fig. 8(d) most of the $D_{50, rBCc}$ was around 200 nm
429 which illustrates that the number concentrations of rBCc with D_a above 200 nm had
430 significant contribution to the overall AF_{rBCc} .

431

432 Fig. 8(b) presents the temporal evolution of the CCN number concentration and
433 activation fraction for all particles and rBCc. Fig. 8(e) showed $50 \pm 4\%$ of the measured
434 particles can be activated with $SS=0.2\%$ under heavy polluted period, while the AF_{all}
435 for the light pollution period was generally lower than the AF_{all} of the other two periods
436 which was $24 \pm 10\%$ on average. The AF_{all} for the moderate pollution period was $39 \pm$
437 9% on average. Shown in Fig. 8(e) and (f), both all particles and rBCc showed high
438 activation fraction of around 50% during the heavy pollution periods. While for
439 moderate and light pollution conditions, rBCc exhibited substantially higher activation



440 fraction than all particles, especially under light pollution periods where the average
441 activation fraction was $44 \pm 18\%$ for rBCc compared to $24 \pm 10\%$ for all particles. The
442 maintaining high rBCc activation fraction at all pollution levels resulted from the
443 relatively higher rBC number fractions at larger D_a (Fig. 8(c)) because of the higher
444 associated coatings. The directly measured CCN activity of rBCc showed that particles
445 at larger sizes had contained a larger fraction of rBCc that were CCN active, due to the
446 larger particle size. This in turn implies that the rBCc has the potential to be more
447 efficiently incorporated into cloud droplets. The measured and modelled AF_{rBCc} was
448 close and agreed within 22% (shown in Fig. S3), and the modelled AF_{rBCc} was slightly
449 higher than the measurement results. This underestimation of modelled $D_{50, \text{rBCc}}$ may
450 result from an overestimation on the κ_{rBCc} as here a consistent κ was applied between
451 rBCc coatings and all non-refractory materials in bulk, though the coatings on rBC may
452 have not contained as much hygroscopic materials as the bulk non-rBC aerosols.
453 Freshly emitted rBC particles contain substantial amounts of organic matter (Peng et
454 al., 2017) while the more hygroscopic secondary inorganic materials require
455 atmospheric aging to be mixed with rBC (Hu et al., 2020a). Our results confirm that
456 while rBCc can be CCN active, and the size of rBCc is crucial to the rBCc CCN ability
457 in polluted suburban environment. This AF_{rBCc} result presented here is generally
458 consistent with previous field measurements: Wu et al. (2019) and Hu et al. (2021)
459 reported 59% and 60% of total rBCc could be activated with $SS = 0.2\%$ respectively in
460 other anthropogenic polluted environment.

461

462 **4. Atmospheric implications**

463 The AAC combination applied in this study introduced a new way to explore the
464 physiochemical properties of aerosols. The comprehensive size-resolved aerosol
465 information presented in this study can contribute to future studies focusing on the BC
466 evolution and lifetime, and improve the particle resolved model simulations (i.e.
467 Riemer et al. (2009)) for the anthropogenic polluted environment. Importantly, our
468 results shown that thickly coated rBCc accounted higher number fraction at larger
469 particle size than the smaller particle size in Beijing suburban. As indicated in Fig. 9,
470 the mass absorption coefficient (MAC) of rBCc at 880nm wavelength is calculated
471 through the core-shell Mie model described in the supplementary. The MAC_{880} was
472 largely enhanced for rBCc with $D_a > 500$ nm. These larger rBCc with higher absorption



473 efficiency importantly contributed to the total absorption. When transported into the
474 top of boundary layer, these highly coated and absorbing rBCc can be efficiently
475 incorporated into clouds (Ding et al., 2019). The absorption effects of these rBCc will
476 be further magnified by mixing with the cloud water droplets (Wu et al., 2016), and the
477 lensing effect may reduce the cloud lifetime (Ramanathan et al., 2001) or the cloud
478 albedo (Chuang et al., 2002). In addition to the strong radiative absorption, these large
479 rBCc may also alter the regional precipitation rate (Johnson et al., 2019).

480

481 **Conclusions**

482 In this study, a new aerodynamic size selection technique was applied for the direct
483 size-resolved characterisation of aerosol constituents and properties on both mass and
484 number basis in a suburban Beijing in winter. Besides the size selection without relying
485 on particle charging efficiency, this technique allows reliable size-resolved particle
486 properties. Organic compound accounted around 40% of the total PM₁ mass, and we
487 found higher contribution of particulate nitrate at larger sizes under polluted cases in
488 Beijing suburban. In particular, particles with larger aerodynamic diameter (D_a) were
489 found to contain a higher number fraction of refractory black carbon (rBC), which
490 means rBC could be more efficiently mixed with larger particles during atmospheric
491 processes. Mie calculation results show that these thickly coated rBC containing
492 particles (rBCc) as included in large particle may have an up to 2-fold of enhanced
493 absorption. The dynamic shape factors for both refractory and non-refractory particles
494 have also been derived. Particles with D_a larger than 300 nm tended to have a more
495 spherical-like shape, while smaller particles were with more irregular shape in the
496 polluted environment. By applying the method introduced by Hu et al. (2021), as high
497 as $46 \pm 15\%$ number fraction of rBCc was observed to be activated under SS=0.2%.
498 Our results suggest that the size of rBCc is key to the cloud condensation nuclei (CCN)
499 activities of rBCc. Though rBC was small and hydrophobic initially, after being mixed
500 with non-refractory compositions and becoming larger, the rBCc can become CCN
501 active. The higher number fraction of rBCc at larger particle size ($D_a > 300$ nm)
502 emphasizes the importance of the rBCc as a considerable CCN source. In summary, the
503 rBCc from anthropogenic emissions, after short aging in regional scale, may therefore
504 alter the regional radiative forcing directly or indirectly through altering cloud
505 properties and deposit on human respiratory system efficiently.



506

507 Acknowledgments

508 This research was supported by the National Key Research and Development Program
509 of China (2016YFA0602001, 2019YFC0214703) and the National Natural Science
510 Foundation of China (41875167). The authors acknowledge the Cambustion Ltd for
511 providing the AAC instrument.

512

513 Author Contribution

514 CY and DL deigned the experiments and wrote the paper; DL and JDA provided
515 guidance with the analysis and writing; CY, DL, KH, PT, YW, DZ, WG, MH and DD
516 performed experiments; CY, DL, KH, HW, DH and JDA contributed to the data
517 analysis; QL provided the AAC and guided the operations.

518

519 Data availability

520 Raw data is archived at Zhejiang University and is available on request.

521

522 Competing financial interests

523 The authors declare no competing financial interests.

524

525 References

- 526 Ahern, A. T., Subramanian, R., Saliba, G., Lipsky, E. M., Donahue, N. M., and
527 Sullivan, R. C.: Effect of secondary organic aerosol coating thickness on the real-time
528 detection and characterization of biomass-burning soot by two particle mass
529 spectrometers, *Atmos. Meas. Tech.*, 9, 6117-6137, 10.5194/amt-9-6117-2016, 2016.
530 Bessho, K., Date, K., Hayashi, M., Ikeda, A., Imai, T., Inoue, H., Kumagai, Y.,
531 Miyakawa, T., Murata, H., Ohno, T., Okuyama, A., Oyama, R., Sasaki, Y., Shimazu,
532 Y., Shimoji, K., Sumida, Y., Suzuki, M., Taniguchi, H., Tsuchiyama, H., Uesawa, D.,
533 Yokota, H., and Yoshida, R.: An Introduction to Himawari-8/9—
534 Japan's New-Generation Geostationary Meteorological Satellites, *Journal of
535 the Meteorological Society of Japan. Ser. II*, 94, 151-183, 10.2151/jmsj.2016-009,
536 2016.
537 Bond, T. C., Doherty, S. J., Fahey, D. W., Forster, P. M., Berntsen, T., DeAngelo, B.
538 J., Flanner, M. G., Ghan, S., Kärcher, B., Koch, D., Kinne, S., Kondo, Y., Quinn, P.
539 K., Sarofim, M. C., Schultz, M. G., Schulz, M., Venkataraman, C., Zhang, H., Zhang,
540 S., Bellouin, N., Guttikunda, S. K., Hopke, P. K., Jacobson, M. Z., Kaiser, J. W.,
541 Klimont, Z., Lohmann, U., Schwarz, J. P., Shindell, D., Storelvmo, T., Warren, S. G.,
542 and Zender, C. S.: Bounding the role of black carbon in the climate system: A
543 scientific assessment, *Journal of Geophysical Research: Atmospheres*, 118, 5380-



- 544 5552, <https://doi.org/10.1002/jgrd.50171>, 2013.
- 545 Broekhuizen, K., Chang, R. Y. W., Leaitch, W. R., Li, S. M., and Abbatt, J. P. D.:
- 546 Closure between measured and modeled cloud condensation nuclei (CCN) using size-
- 547 resolved aerosol compositions in downtown Toronto, *Atmos. Chem. Phys.*, 6, 2513-
- 548 2524, 10.5194/acp-6-2513-2006, 2006.
- 549 Brown, A., Milton, S., Cullen, M., Golding, B., Mitchell, J., and Shelly, A.: Unified
- 550 Modeling and Prediction of Weather and Climate: A 25-Year Journey, *Bulletin of the*
- 551 *American Meteorological Society*, 93, 1865-1877, 10.1175/BAMS-D-12-00018.1,
- 552 2012.
- 553 Cappa, C. D., Onasch, T. B., Massoli, P., Worsnop, D. R., Bates, T. S., Cross, E. S.,
- 554 Davidovits, P., Hakala, J., Hayden, K. L., Jobson, B. T., Kolesar, K. R., Lack, D. A.,
- 555 Lerner, B. M., Li, S.-M., Mellon, D., Nuaaman, I., Olfert, J. S., Petäjä, T., Quinn, P.
- 556 K., Song, C., Subramanian, R., Williams, E. J., and Zaveri, R. A.: Radiative
- 557 Absorption Enhancements Due to the Mixing State of Atmospheric Black Carbon,
- 558 *Science*, 337, 1078, 10.1126/science.1223447, 2012.
- 559 Carvalho, T. C., Peters, J. I., and Williams, R. O.: Influence of particle size on
- 560 regional lung deposition – What evidence is there?, *International Journal of*
- 561 *Pharmaceutics*, 406, 1-10, <https://doi.org/10.1016/j.ijpharm.2010.12.040>, 2011.
- 562 Chen, Y., Cai, J., Wang, Z., Peng, C., Yao, X., Tian, M., Han, Y., Shi, G., Shi, Z.,
- 563 Liu, Y., Yang, X., Zheng, M., Zhu, T., He, K., Zhang, Q., and Yang, F.: Simultaneous
- 564 measurements of urban and rural particles in Beijing – Part 1: Chemical composition
- 565 and mixing state, *Atmos. Chem. Phys.*, 20, 9231-9247, 10.5194/acp-20-9231-2020,
- 566 2020a.
- 567 Chen, Y., Shi, G., Cai, J., Shi, Z., Wang, Z., Yao, X., Tian, M., Peng, C., Han, Y.,
- 568 Zhu, T., Liu, Y., Yang, X., Zheng, M., Yang, F., Zhang, Q., and He, K.: Simultaneous
- 569 measurements of urban and rural particles in Beijing – Part 2: Case studies of haze
- 570 events and regional transport, *Atmos. Chem. Phys.*, 20, 9249-9263, 10.5194/acp-20-
- 571 9249-2020, 2020b.
- 572 Chuang, C. C., Penner, J. E., Prospero, J. M., Grant, K. E., Rau, G. H., and
- 573 Kawamoto, K.: Cloud susceptibility and the first aerosol indirect forcing: Sensitivity
- 574 to black carbon and aerosol concentrations, *Journal of Geophysical Research:*
- 575 *Atmospheres*, 107, AAC 10-11-AAC 10-23, <https://doi.org/10.1029/2000JD000215>,
- 576 2002.
- 577 DeCarlo, P. F., Slowik, J. G., Worsnop, D. R., Davidovits, P., and Jimenez, J. L.:
- 578 Particle Morphology and Density Characterization by Combined Mobility and
- 579 Aerodynamic Diameter Measurements. Part 1: Theory, *Aerosol Science and*
- 580 *Technology*, 38, 1185-1205, 10.1080/027868290903907, 2004.
- 581 DeCarlo, P. F., Kimmel, J. R., Trimborn, A., Northway, M. J., Jayne, J. T., Aiken, A.
- 582 C., Gonin, M., Fuhrer, K., Horvath, T., Docherty, K. S., Worsnop, D. R., and Jimenez,
- 583 J. L.: Field-Deployable, High-Resolution, Time-of-Flight Aerosol Mass Spectrometer,
- 584 *Analytical Chemistry*, 78, 8281-8289, 10.1021/ac061249n, 2006.
- 585 Ding, S., Liu, D., Zhao, D., Hu, K., Tian, P., Zhou, W., Huang, M., Yang, Y., Wang,
- 586 F., Sheng, J., Liu, Q., Kong, S., Cui, P., Huang, Y., He, H., Coe, H., and Ding, D.:
- 587 Size-Related Physical Properties of Black Carbon in the Lower Atmosphere over
- 588 Beijing and Europe, *Environmental Science & Technology*, 53, 11112-11121,
- 589 10.1021/acs.est.9b03722, 2019.
- 590 Fierce, L., Onasch, T. B., Cappa, C. D., Mazzoleni, C., China, S., Bhandari, J.,
- 591 Davidovits, P., Fischer, D. A., Helgestad, T., Lambe, A. T., Sedlacek, A. J., Smith, G.
- 592 D., and Wolff, L.: Radiative absorption enhancements by black carbon controlled by
- 593 particle-to-particle heterogeneity in composition, *Proceedings of the National*



- 594 Academy of Sciences, 117, 5196, 10.1073/pnas.1919723117, 2020.
- 595 Fukuda, S., Nakajima, T., Takenaka, H., Higurashi, A., Kikuchi, N., Nakajima, T. Y.,
596 and Ishida, H.: New approaches to removing cloud shadows and evaluating the
597 380 nm surface reflectance for improved aerosol optical thickness retrievals from the
598 GOSAT/TANSO-Cloud and Aerosol Imager, *Journal of Geophysical Research: Atmospheres*, 118, 13,520-513,531, <https://doi.org/10.1002/2013JD020090>, 2013.
- 599 Gysel, M., Crosier, J., Topping, D. O., Whitehead, J. D., Bower, K. N., Cubison, M.
600 J., Williams, P. I., Flynn, M. J., McFiggans, G. B., and Coe, H.: Closure study
601 between chemical composition and hygroscopic growth of aerosol particles during
602 TORCH2, *Atmos. Chem. Phys.*, 7, 6131-6144, 10.5194/acp-7-6131-2007, 2007.
- 603 Han, C., Li, S. M., Liu, P., and Lee, P.: Size Dependence of the Physical
604 Characteristics of Particles Containing Refractory Black Carbon in Diesel Vehicle
605 Exhaust, *Environ Sci Technol*, 53, 137-145, 10.1021/acs.est.8b04603, 2019.
- 606 Han, Y., Chen, W., Chatzidiakou, L., Krause, A., Yan, L., Zhang, H., Chan, Q.,
607 Barratt, B., Jones, R., Liu, J., Wu, Y., Zhao, M., Zhang, J., Kelly, F. J., Zhu, T., and
608 the, A. t.: Effects of AIR pollution on cardiopulmonary disease in urban and peri-
609 urban residents in Beijing: protocol for the AIRLESS study, *Atmos. Chem. Phys.*, 20,
610 15775-15792, 10.5194/acp-20-15775-2020, 2020.
- 611 Hu, D., Liu, D., Zhao, D., Yu, C., Liu, Q., Tian, P., Bi, K., Ding, S., Hu, K., Wang, F.,
612 Wu, Y., Wu, Y., Kong, S., Zhou, W., He, H., Huang, M., and Ding, D.: Closure
613 Investigation on Cloud Condensation Nuclei Ability of Processed Anthropogenic
614 Aerosols, *Journal of Geophysical Research: Atmospheres*, 125,
615 10.1029/2020jd032680, 2020a.
- 616 Hu, D., Wang, Y., Yu, C., Xie, Q., Yue, S., Shang, D., Fang, X., Joshi, R., Liu, D.,
617 Allan, J., Wu, Z., Hu, M., Fu, P., and McFiggans, G.: Vertical profile of particle
618 hygroscopicity and CCN effectiveness during winter in Beijing: insight into the
619 hygroscopicity transition threshold of black carbon, *Faraday Discuss*,
620 10.1039/d0fd00077a, 2020b.
- 621 Hu, D., Liu, D., Kong, S., Zhao, D., Wu, Y., Li, S., Ding, S., Zheng, S., Cheng, Y.,
622 Hu, K., Deng, Z., Wu, Y., Tian, P., Liu, Q., Huang, M., and Ding, D.: Direct
623 Quantification of Droplet Activation of Ambient Black Carbon Under Water
624 Supersaturation, *Journal of Geophysical Research: Atmospheres*, 126,
625 e2021JD034649, <https://doi.org/10.1029/2021JD034649>, 2021.
- 626 Hu, W., Hu, M., Hu, W., Jimenez, J. L., Yuan, B., Chen, W., Wang, M., Wu, Y.,
627 Chen, C., Wang, Z., Peng, J., Zeng, L., and Shao, M.: Chemical composition, sources,
628 and aging process of submicron aerosols in Beijing: Contrast between summer and
629 winter, *Journal of Geophysical Research: Atmospheres*, 121, 1955-1977,
630 <https://doi.org/10.1002/2015JD024020>, 2016.
- 631 Johnson, B. T., Haywood, J. M., and Hawcroft, M. K.: Are Changes in Atmospheric
632 Circulation Important for Black Carbon Aerosol Impacts on Clouds, Precipitation, and
633 Radiation?, *Journal of Geophysical Research: Atmospheres*, 124, 7930-7950,
634 <https://doi.org/10.1029/2019JD030568>, 2019.
- 635 Johnson, T. J., Irwin, M., Symonds, J. P. R., Olfert, J. S., and Boies, A. M.:
636 Measuring aerosol size distributions with the aerodynamic aerosol classifier, *Aerosol
637 Science and Technology*, 52, 655-665, 10.1080/02786826.2018.1440063, 2018.
- 638 Jones, A., Thomson, D., Hort, M., and Devenish, B.: The U.K. Met Office's Next-
639 Generation Atmospheric Dispersion Model, NAME III, *Air Pollution Modeling and
640 Its Application XVII*, Boston, MA, 2007, 580-589.
- 641 Joshi, R., Liu, D., Nemitz, E., Langford, B., Mullinger, N., Squires, F., Lee, J., Wu,
642 Y., Pan, X., Fu, P., Kotthaus, S., Grimmond, S., Zhang, Q., Wu, R., Wild, O., Flynn,



- 644 M., Coe, H., and Allan, J.: Direct measurements of black carbon fluxes in central
645 Beijing using the eddy covariance method, *Atmospheric Chemistry and Physics*, 21,
646 147-162, 10.5194/acp-21-147-2021, 2021.
- 647 Kim, J. H., Mulholland, G. W., Kukuck, S. R., and Pui, D. Y. H.: Slip Correction
648 Measurements of Certified PSL Nanoparticles Using a Nanometer Differential
649 Mobility Analyzer (Nano-DMA) for Knudsen Number From 0.5 to 83, *J Res Natl Inst*
650 *Stand Technol*, 110, 31-54, 10.6028/jres.110.005, 2005.
- 651 Kwon, H.-S., Ryu, M. H., and Carlsten, C.: Ultrafine particles: unique
652 physicochemical properties relevant to health and disease, *Experimental & Molecular*
653 *Medicine*, 52, 318-328, 10.1038/s12276-020-0405-1, 2020.
- 654 Laborde, M., Schnaiter, M., Linke, C., Saathoff, H., Naumann, K. H., Möhler, O.,
655 Berlenz, S., Wagner, U., Taylor, J. W., Liu, D., Flynn, M., Allan, J. D., Coe, H.,
656 Heimerl, K., Dahlkötter, F., Weinzierl, B., Wollny, A. G., Zanatta, M., Cozic, J., Laj,
657 P., Hitznerberger, R., Schwarz, J. P., and Gysel, M.: Single Particle Soot Photometer
658 intercomparison at the AIDA chamber, *Atmos. Meas. Tech.*, 5, 3077-3097,
659 10.5194/amt-5-3077-2012, 2012.
- 660 Lack, D. A., and Cappa, C. D.: Impact of brown and clear carbon on light absorption
661 enhancement, single scatter albedo and absorption wavelength dependence of black
662 carbon, *Atmos. Chem. Phys.*, 10, 4207-4220, 10.5194/acp-10-4207-2010, 2010.
- 663 Levin, E. J. T., Prenni, A. J., Palm, B. B., Day, D. A., Campuzano-Jost, P., Winkler,
664 P. M., Kreidenweis, S. M., DeMott, P. J., Jimenez, J. L., and Smith, J. N.: Size-
665 resolved aerosol composition and its link to hygroscopicity at a forested site in
666 Colorado, *Atmos. Chem. Phys.*, 14, 2657-2667, 10.5194/acp-14-2657-2014, 2014.
- 667 Li, H., Zhang, Q., Zheng, B., Chen, C., Wu, N., Guo, H., Zhang, Y., Zheng, Y., Li,
668 X., and He, K.: Nitrate-driven urban haze pollution during summertime over the
669 North China Plain, *Atmos. Chem. Phys.*, 18, 5293-5306, 10.5194/acp-18-5293-2018,
670 2018.
- 671 Li, J., Cao, L., Gao, W., He, L., Yan, Y., He, Y., Pan, Y., Ji, D., Liu, Z., and Wang,
672 Y.: Seasonal variations in the highly time-resolved aerosol composition, sources and
673 chemical processes of background submicron particles in the North China Plain,
674 *Atmospheric Chemistry and Physics*, 21, 4521-4539, 10.5194/acp-21-4521-2021,
675 2021.
- 676 Lin, G.-Y., Lee, G.-R., Lin, S.-F., Hung, Y.-H., Li, S.-W., Wu, G.-J., Ye, H., Huang,
677 W., and Tsai, C.-J.: Ultrafine Particles and PM_{2.5} at Three Urban Air Monitoring
678 Stations in Northern Taiwan from 2011 to 2013, *Aerosol and Air Quality Research*,
679 15, 2305-2317, 10.4209/aaqr.2015.04.0271, 2015.
- 680 Lipworth, B., Manoharan, A., and Anderson, W.: Unlocking the quiet zone: the small
681 airway asthma phenotype, *The Lancet Respiratory Medicine*, 2, 497-506,
682 [https://doi.org/10.1016/S2213-2600\(14\)70103-1](https://doi.org/10.1016/S2213-2600(14)70103-1), 2014.
- 683 Liu, D., Allan, J., Whitehead, J., Young, D., Flynn, M., Coe, H., McFiggans, G.,
684 Fleming, Z. L., and Bandy, B.: Ambient black carbon particle hygroscopic properties
685 controlled by mixing state and composition, *Atmos. Chem. Phys.*, 13, 2015-2029,
686 10.5194/acp-13-2015-2013, 2013.
- 687 Liu, D., Quennehen, B., Darbyshire, E., Allan, J. D., Williams, P. I., Taylor, J. W.,
688 Bauguitte, S. J. B., Flynn, M. J., Lowe, D., Gallagher, M. W., Bower, K. N.,
689 Choularton, T. W., and Coe, H.: The importance of Asia as a source of black carbon
690 to the European Arctic during springtime 2013, *Atmos. Chem. Phys.*, 15, 11537-
691 11555, 10.5194/acp-15-11537-2015, 2015.
- 692 Liu, D., Whitehead, J., Alfarra, M. R., Reyes-Villegas, E., Spracklen, Dominick V.,
693 Reddington, Carly L., Kong, S., Williams, Paul I., Ting, Y.-C., Haslett, S., Taylor,



- 694 Jonathan W., Flynn, Michael J., Morgan, William T., McFiggans, G., Coe, H., and
695 Allan, James D.: Black-carbon absorption enhancement in the atmosphere determined
696 by particle mixing state, *Nature Geoscience*, 10, 184-188, 10.1038/ngeo2901, 2017.
697 Liu, D., Joshi, R., Wang, J., Yu, C., Allan, J. D., Coe, H., Flynn, M. J., Xie, C., Lee,
698 J., Squires, F., Kotthaus, S., Grimmond, S., Ge, X., Sun, Y., and Fu, P.: Contrasting
699 physical properties of black carbon in urban Beijing between winter and summer,
700 *Atmos. Chem. Phys.*, 19, 6749-6769, 10.5194/acp-19-6749-2019, 2019.
701 Liu, D., He, C., Schwarz, J. P., and Wang, X.: Lifecycle of light-absorbing
702 carbonaceous aerosols in the atmosphere, *npj Climate and Atmospheric Science*, 3,
703 10.1038/s41612-020-00145-8, 2020.
704 Liu, Q., Liu, D., Wu, Y., Bi, K., Gao, W., Tian, P., Zhao, D., Li, S., Yu, C., Wu, Y.,
705 Hu, K., Ding, S., Gao, Q., Wang, F., He, H., Huang, M., and Ding, D.: Reduced
706 volatility of aerosols from surface emission to the top of planetary boundary layer,
707 *Atmos. Chem. Phys. Discuss.*, 2021, 1-19, 10.5194/acp-2021-362, 2021.
708 Liu, Z., Hu, B., Zhang, J., Yu, Y., and Wang, Y.: Characteristics of aerosol size
709 distributions and chemical compositions during wintertime pollution episodes in
710 Beijing, *Atmospheric Research*, 168, 1-12,
711 <https://doi.org/10.1016/j.atmosres.2015.08.013>, 2016.
712 Manigrasso, M., Costabile, F., Liberto, L. D., Gobbi, G. P., Gualtieri, M., Zanini, G.,
713 and Avino, P.: Size resolved aerosol respiratory doses in a Mediterranean urban area:
714 From PM10 to ultrafine particles, *Environment International*, 141, 105714,
715 <https://doi.org/10.1016/j.envint.2020.105714>, 2020.
716 Marple, V. A., Rubow, K. L., and Behm, S. M.: A Microorifice Uniform Deposit
717 Impactor (MOUDI): Description, Calibration, and Use, *Aerosol Science and*
718 *Technology*, 14, 434-446, 10.1080/02786829108959504, 1991.
719 Matsui, H., Hamilton, D. S., and Mahowald, N. M.: Black carbon radiative effects
720 highly sensitive to emitted particle size when resolving mixing-state diversity, *Nature*
721 *Communications*, 9, 3446, 10.1038/s41467-018-05635-1, 2018.
722 Middlebrook, A. M., Bahreini, R., Jimenez, J. L., and Canagaratna, M. R.: Evaluation
723 of Composition-Dependent Collection Efficiencies for the Aerodyne Aerosol Mass
724 Spectrometer using Field Data, *Aerosol Science and Technology*, 46, 258-271,
725 10.1080/02786826.2011.620041, 2012.
726 Motos, G., Schmale, J., Corbin, J. C., Modini, R. L., Karlen, N., Bertò, M.,
727 Baltensperger, U., and Gysel-Beer, M.: Cloud droplet activation properties and
728 scavenged fraction of black carbon in liquid-phase clouds at the high-alpine research
729 station Jungfraujoch (3580&thinspm&thinspa.s.l.), *Atmos. Chem. Phys.*, 19, 3833-
730 3855, 10.5194/acp-19-3833-2019, 2019.
731 Myhre, G., and Samset, B. H.: Standard climate models radiation codes underestimate
732 black carbon radiative forcing, *Atmos. Chem. Phys.*, 15, 2883-2888, 10.5194/acp-15-
733 2883-2015, 2015.
734 Peng, J., Hu, M., Guo, S., Du, Z., Zheng, J., Shang, D., Levy Zamora, M., Zeng, L.,
735 Shao, M., Wu, Y.-S., Zheng, J., Wang, Y., Glen, C. R., Collins, D. R., Molina, M. J.,
736 and Zhang, R.: Markedly enhanced absorption and direct radiative forcing of black
737 carbon under polluted urban environments, *Proceedings of the National Academy of*
738 *Sciences*, 113, 4266, 10.1073/pnas.1602310113, 2016.
739 Peng, J., Hu, M., Guo, S., Du, Z., Shang, D., Zheng, J., Zheng, J., Zeng, L., Shao, M.,
740 Wu, Y., Collins, D., and Zhang, R.: Ageing and hygroscopicity variation of black
741 carbon particles in Beijing measured by a quasi-atmospheric aerosol evolution study
742 (QUALITY) chamber, *Atmos. Chem. Phys.*, 17, 10333-10348, 10.5194/acp-17-
743 10333-2017, 2017.



- 744 Petters, M. D., and Kreidenweis, S. M.: A single parameter representation of
745 hygroscopic growth and cloud condensation nucleus activity, *Atmos. Chem. Phys.*, 7,
746 1961-1971, 10.5194/acp-7-1961-2007, 2007.
- 747 Ramanathan, V., Crutzen, P. J., Kiehl, J. T., and Rosenfeld, D.: Aerosols, Climate,
748 and the Hydrological Cycle, *Science*, 294, 2119, 10.1126/science.1064034, 2001.
- 749 Ravishankara, A. R., Rudich, Y., and Wuebbles, D. J.: *Physical Chemistry of Climate*
750 Metrics, *Chemical Reviews*, 115, 3682-3703, 10.1021/acs.chemrev.5b00010, 2015.
- 751 Reddington, C. L., McMeeking, G., Mann, G. W., Coe, H., Frontoso, M. G., Liu, D.,
752 Flynn, M., Spracklen, D. V., and Carslaw, K. S.: The mass and number size
753 distributions of black carbon aerosol over Europe, *Atmos. Chem. Phys.*, 13, 4917-
754 4939, 10.5194/acp-13-4917-2013, 2013.
- 755 Riemer, N., West, M., Zaveri, R. A., and Easter, R. C.: Simulating the evolution of
756 soot mixing state with a particle-resolved aerosol model, *Journal of Geophysical*
757 *Research*, 114, 10.1029/2008jd011073, 2009.
- 758 Riemer, N., Ault, A. P., West, M., Craig, R. L., and Curtis, J. H.: Aerosol Mixing
759 State: Measurements, Modeling, and Impacts, *Reviews of Geophysics*, 57, 187-249,
760 10.1029/2018rg000615, 2019.
- 761 Rissler, J., Gudmundsson, A., Nicklasson, H., Swietlicki, E., Wollmer, P., and
762 Löndahl, J.: Deposition efficiency of inhaled particles (15-5000 nm) related to
763 breathing pattern and lung function: an experimental study in healthy children and
764 adults, *Part Fibre Toxicol*, 14, 10-10, 10.1186/s12989-017-0190-8, 2017.
- 765 Schwarz, J. P., Spackman, J. R., Gao, R. S., Perring, A. E., Cross, E., Onasch, T. B.,
766 Ahern, A., Wrobel, W., Davidovits, P., Olfert, J., Dubey, M. K., Mazzoleni, C., and
767 Fahey, D. W.: The Detection Efficiency of the Single Particle Soot Photometer,
768 *Aerosol Science and Technology*, 44, 612-628, 10.1080/02786826.2010.481298,
769 2010.
- 770 Shi, Z., Vu, T., Kotthaus, S., Harrison, R. M., Grimmond, S., Yue, S., Zhu, T., Lee, J.,
771 Han, Y., Demuzere, M., Dunmore, R. E., Ren, L., Liu, D., Wang, Y., Wild, O., Allan,
772 J., Acton, W. J., Barlow, J., Barratt, B., Beddows, D., Bloss, W. J., Calzolari, G.,
773 Carruthers, D., Carslaw, D. C., Chan, Q., Chatzidiakou, L., Chen, Y., Crilley, L., Coe,
774 H., Dai, T., Doherty, R., Duan, F., Fu, P., Ge, B., Ge, M., Guan, D., Hamilton, J. F.,
775 He, K., Heal, M., Heard, D., Hewitt, C. N., Holloway, M., Hu, M., Ji, D., Jiang, X.,
776 Jones, R., Kalberer, M., Kelly, F. J., Kramer, L., Langford, B., Lin, C., Lewis, A. C.,
777 Li, J., Li, W., Liu, H., Liu, J., Loh, M., Lu, K., Lucarelli, F., Mann, G., McFiggans,
778 G., Miller, M. R., Mills, G., Monk, P., Nemitz, E., O'Connor, F., Ouyang, B., Palmer,
779 P. I., Percival, C., Popoola, O., Reeves, C., Rickard, A. R., Shao, L., Shi, G.,
780 Spracklen, D., Stevenson, D., Sun, Y., Sun, Z., Tao, S., Tong, S., Wang, Q., Wang,
781 W., Wang, X., Wang, X., Wang, Z., Wei, L., Whalley, L., Wu, X., Wu, Z., Xie, P.,
782 Yang, F., Zhang, Q., Zhang, Y., Zhang, Y., and Zheng, M.: Introduction to the special
783 issue "In-depth study of air pollution sources and processes within Beijing and its
784 surrounding region (APHH-Beijing)", *Atmos. Chem. Phys.*, 19, 7519-7546,
785 10.5194/acp-19-7519-2019, 2019.
- 786 Squires, F. A., Nemitz, E., Langford, B., Wild, O., Drysdale, W. S., Acton, W. J. F.,
787 Fu, P., Grimmond, C. S. B., Hamilton, J. F., Hewitt, C. N., Holloway, M., Kotthaus,
788 S., Lee, J., Metzger, S., Pinguha-Durden, N., Shaw, M., Vaughan, A. R., Wang, X.,
789 Wu, R., Zhang, Q., and Zhang, Y.: Measurements of traffic-dominated pollutant
790 emissions in a Chinese megacity, *Atmos. Chem. Phys.*, 20, 8737-8761, 10.5194/acp-
791 20-8737-2020, 2020.
- 792 Stokes, R. H., and Robinson, R. A.: Interactions in Aqueous Nonelectrolyte Solutions.
793 I. Solute-Solvent Equilibria, *The Journal of Physical Chemistry*, 70, 2126-2131,



794 10.1021/j100879a010, 1966.
795 Sturm, R.: Theoretical models for dynamic shape factors and lung deposition of small
796 particle aggregates originating from combustion processes, *Zeitschrift für*
797 *Medizinische Physik*, 20, 226-234, <https://doi.org/10.1016/j.zemedi.2010.04.001>,
798 2010.
799 Sturm, R.: Computer-aided generation and lung deposition modeling of nano-scale
800 particle aggregates, *Inhalation Toxicology*, 29, 160-168,
801 10.1080/08958378.2017.1329362, 2017.
802 Sun, J., Liu, L., Xu, L., Wang, Y., Wu, Z., Hu, M., Shi, Z., Li, Y., Zhang, X., Chen,
803 J., and Li, W.: Key Role of Nitrate in Phase Transitions of Urban Particles:
804 Implications of Important Reactive Surfaces for Secondary Aerosol Formation,
805 *Journal of Geophysical Research: Atmospheres*, 123, 1234-1243,
806 10.1002/2017jd027264, 2018.
807 Tavakoli, F., and Olfert, J. S.: An Instrument for the Classification of Aerosols by
808 Particle Relaxation Time: Theoretical Models of the Aerodynamic Aerosol Classifier,
809 *Aerosol Science and Technology*, 47, 916-926, 10.1080/02786826.2013.802761,
810 2013.
811 Tavakoli, F., and Olfert, J. S.: Determination of particle mass, effective density,
812 mass–mobility exponent, and dynamic shape factor using an aerodynamic aerosol
813 classifier and a differential mobility analyzer in tandem, *Journal of Aerosol Science*,
814 75, 35-42, <https://doi.org/10.1016/j.jaerosci.2014.04.010>, 2014.
815 Taylor, J. W., Allan, J. D., Allen, G., Coe, H., Williams, P. I., Flynn, M. J., Le Breton,
816 M., Muller, J. B. A., Percival, C. J., Oram, D., Forster, G., Lee, J. D., Rickard, A. R.,
817 Parrington, M., and Palmer, P. I.: Size-dependent wet removal of black carbon in
818 Canadian biomass burning plumes, *Atmos. Chem. Phys.*, 14, 13755-13771,
819 10.5194/acp-14-13755-2014, 2014.
820 Vu, T. V., Zauli-Sajani, S., Poluzzi, V., and Harrison, R. M.: Factors controlling the
821 lung dose of road traffic-generated sub-micrometre aerosols from outdoor to indoor
822 environments, *Air Quality, Atmosphere & Health*, 11, 615-625, 10.1007/s11869-018-
823 0568-2, 2018.
824 Wang, J., Liu, D., Ge, X., Wu, Y., Shen, F., Chen, M., Zhao, J., Xie, C., Wang, Q.,
825 Xu, W., Zhang, J., Hu, J., Allan, J., Joshi, R., Fu, P., Coe, H., and Sun, Y.:
826 Characterization of black carbon-containing fine particles in Beijing during
827 wintertime, *Atmos. Chem. Phys.*, 19, 447-458, 10.5194/acp-19-447-2019, 2019.
828 Wang, J., Ye, J., Liu, D., Wu, Y., Zhao, J., Xu, W., Xie, C., Shen, F., Zhang, J., Ohno,
829 P. E., Qin, Y., Zhao, X., Martin, S. T., Lee, A. K. Y., Fu, P., Jacob, D. J., Zhang, Q.,
830 Sun, Y., Chen, M., and Ge, X.: Characterization of submicron organic particles in
831 Beijing during summertime: comparison between SP-AMS and HR-AMS, *Atmos.*
832 *Chem. Phys.*, 20, 14091-14102, 10.5194/acp-20-14091-2020, 2020.
833 Wang, L., Zhang, F., Pilot, E., Yu, J., Nie, C., Holdaway, J., Yang, L., Li, Y., Wang,
834 W., Vardoulakis, S., and Krafft, T.: Taking Action on Air Pollution Control in the
835 Beijing-Tianjin-Hebei (BTH) Region: Progress, Challenges and Opportunities, *Int J*
836 *Environ Res Public Health*, 15, 10.3390/ijerph15020306, 2018.
837 West, J. J., Cohen, A., Dentener, F., Brunekreef, B., Zhu, T., Armstrong, B., Bell, M.
838 L., Brauer, M., Carmichael, G., Costa, D. L., Dockery, D. W., Kleeman, M.,
839 Krzyzanowski, M., Künzli, N., Liousse, C., Lung, S.-C. C., Martin, R. V., Pöschl, U.,
840 Pope, C. A., Roberts, J. M., Russell, A. G., and Wiedinmyer, C.: “What We Breathe
841 Impacts Our Health: Improving Understanding of the Link between Air Pollution and
842 Health”, *Environmental Science & Technology*, 50, 4895-4904,
843 10.1021/acs.est.5b03827, 2016.



- 844 Wu, Q. Z., Wang, Z. F., Gbaguidi, A., Gao, C., Li, L. N., and Wang, W.: A numerical
845 study of contributions to air pollution in Beijing during CAREBeijing-2006, *Atmos.*
846 *Chem. Phys.*, 11, 5997-6011, 10.5194/acp-11-5997-2011, 2011.
- 847 Wu, Y., Zhang, R., Tian, P., Tao, J., Hsu, S. C., Yan, P., Wang, Q., Cao, J., Zhang,
848 X., and Xia, X.: Effect of ambient humidity on the light absorption amplification of
849 black carbon in Beijing during January 2013, *Atmospheric Environment*, 124, 217-
850 223, <https://doi.org/10.1016/j.atmosenv.2015.04.041>, 2016.
- 851 Wu, Y., Liu, D., Wang, J., Shen, F., Chen, Y., Cui, S., Ge, S., Wu, Y., Chen, M., and
852 Ge, X.: Characterization of Size-Resolved Hygroscopicity of Black Carbon-
853 Containing Particle in Urban Environment, *Environ Sci Technol*, 53, 14212-14221,
854 10.1021/acs.est.9b05546, 2019.
- 855 Xing, Y.-F., Xu, Y.-H., Shi, M.-H., and Lian, Y.-X.: The impact of PM_{2.5} on the
856 human respiratory system, *J Thorac Dis*, 8, E69-E74, 10.3978/j.issn.2072-
857 1439.2016.01.19, 2016.
- 858 Xu, Q., Li, X., Wang, S., Wang, C., Huang, F., Gao, Q., Wu, L., Tao, L., Guo, J.,
859 Wang, W., and Guo, X.: Fine Particulate Air Pollution and Hospital Emergency
860 Room Visits for Respiratory Disease in Urban Areas in Beijing, China, in 2013,
861 *PLOS ONE*, 11, e0153099, 10.1371/journal.pone.0153099, 2016.
- 862 Xu, W., Sun, Y., Wang, Q., Du, W., Zhao, J., Ge, X., Han, T., Zhang, Y., Zhou, W.,
863 Li, J., Fu, P., Wang, Z., and Worsnop, D. R.: Seasonal Characterization of Organic
864 Nitrogen in Atmospheric Aerosols Using High Resolution Aerosol Mass
865 Spectrometry in Beijing, China, *ACS Earth and Space Chemistry*, 1, 673-682,
866 10.1021/acsearthspacechem.7b00106, 2017.
- 867 Yu, C., Liu, D., Broda, K., Joshi, R., Olfert, J., Sun, Y., Fu, P., Coe, H., and Allan, J.
868 D.: Characterising mass-resolved mixing state of black carbon in Beijing using a
869 morphology-independent measurement method, *Atmos. Chem. Phys.*, 20, 3645-3661,
870 10.5194/acp-20-3645-2020, 2020.
- 871 Zhang, J. K., Sun, Y., Liu, Z. R., Ji, D. S., Hu, B., Liu, Q., and Wang, Y. S.:
872 Characterization of submicron aerosols during a month of serious pollution in Beijing,
873 2013, *Atmos. Chem. Phys.*, 14, 2887-2903, 10.5194/acp-14-2887-2014, 2014.
- 874 Zhang, Q., He, K., and Huo, H.: Cleaning China's air, *Nature*, 484, 161-162,
875 10.1038/484161a, 2012.
- 876 Zhang, X. Y., Wang, J. Z., Wang, Y. Q., Liu, H. L., Sun, J. Y., and Zhang, Y. M.:
877 Changes in chemical components of aerosol particles in different haze regions in
878 China from 2006 to 2013 and contribution of meteorological factors, *Atmos. Chem.*
879 *Phys.*, 15, 12935-12952, 10.5194/acp-15-12935-2015, 2015.
- 880 Zhang, Y., Zhang, Q., Cheng, Y., Su, H., Kecorius, S., Wang, Z., Wu, Z., Hu, M.,
881 Zhu, T., Wiedensohler, A., and He, K.: Measuring the morphology and density of
882 internally mixed black carbon with SP2 and VTDMA: new insight into the absorption
883 enhancement of black carbon in the atmosphere, *Atmos. Meas. Tech.*, 9, 1833-1843,
884 10.5194/amt-9-1833-2016, 2016.

885

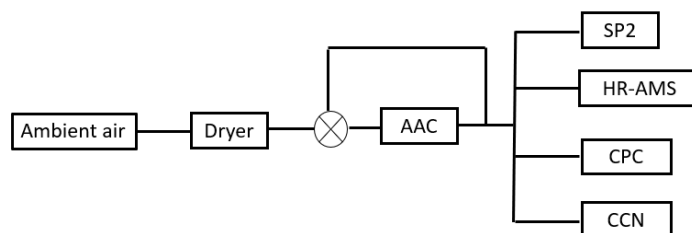
886

887

888



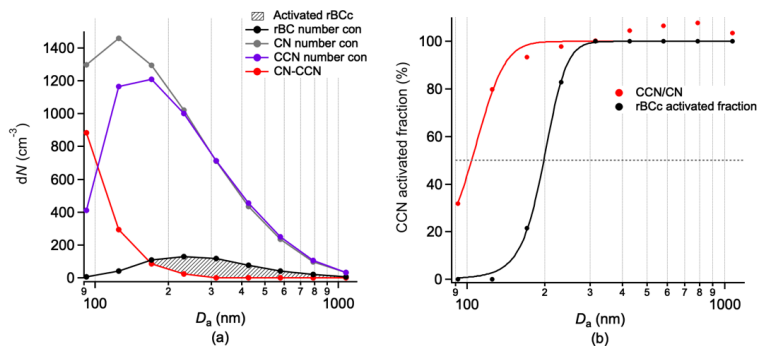
889



890

891 Figure 1. The schematic of the instruments set up. A timed three-way valve was
892 placed at the upstream of the AAC.

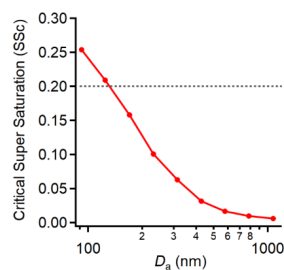
893



894

895 Figure 2 An example of all particles and rBCc activation, the dashed grey line in (b)
896 indicated the 50% of all particles or rBCc activated.

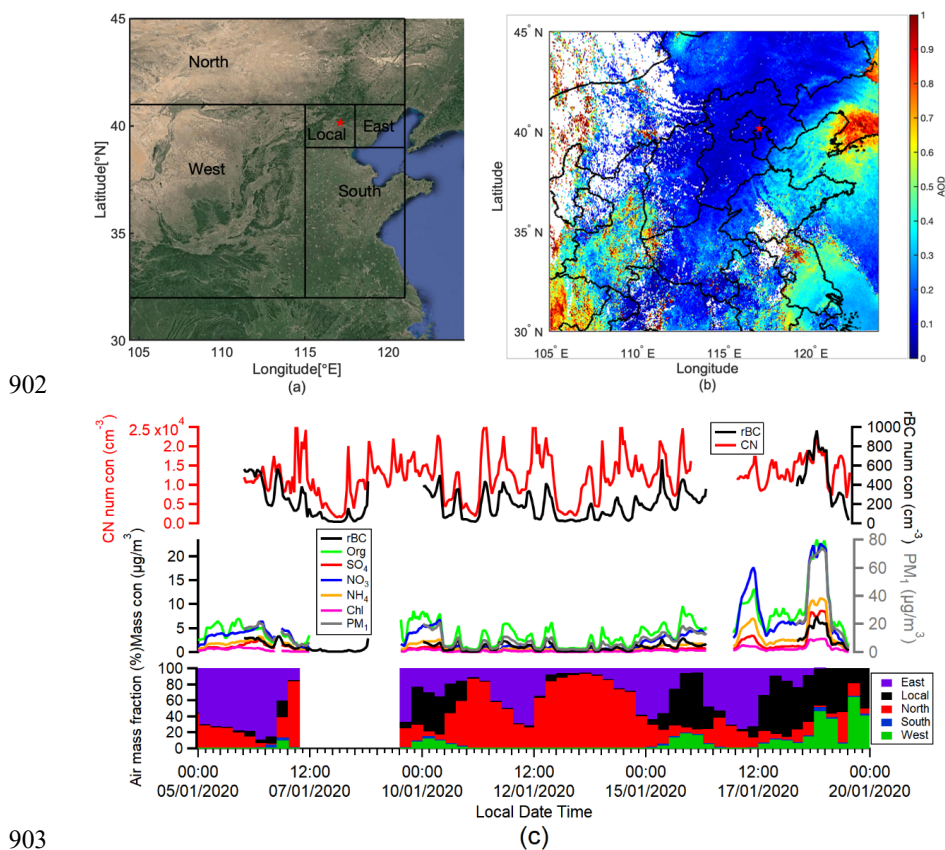
897



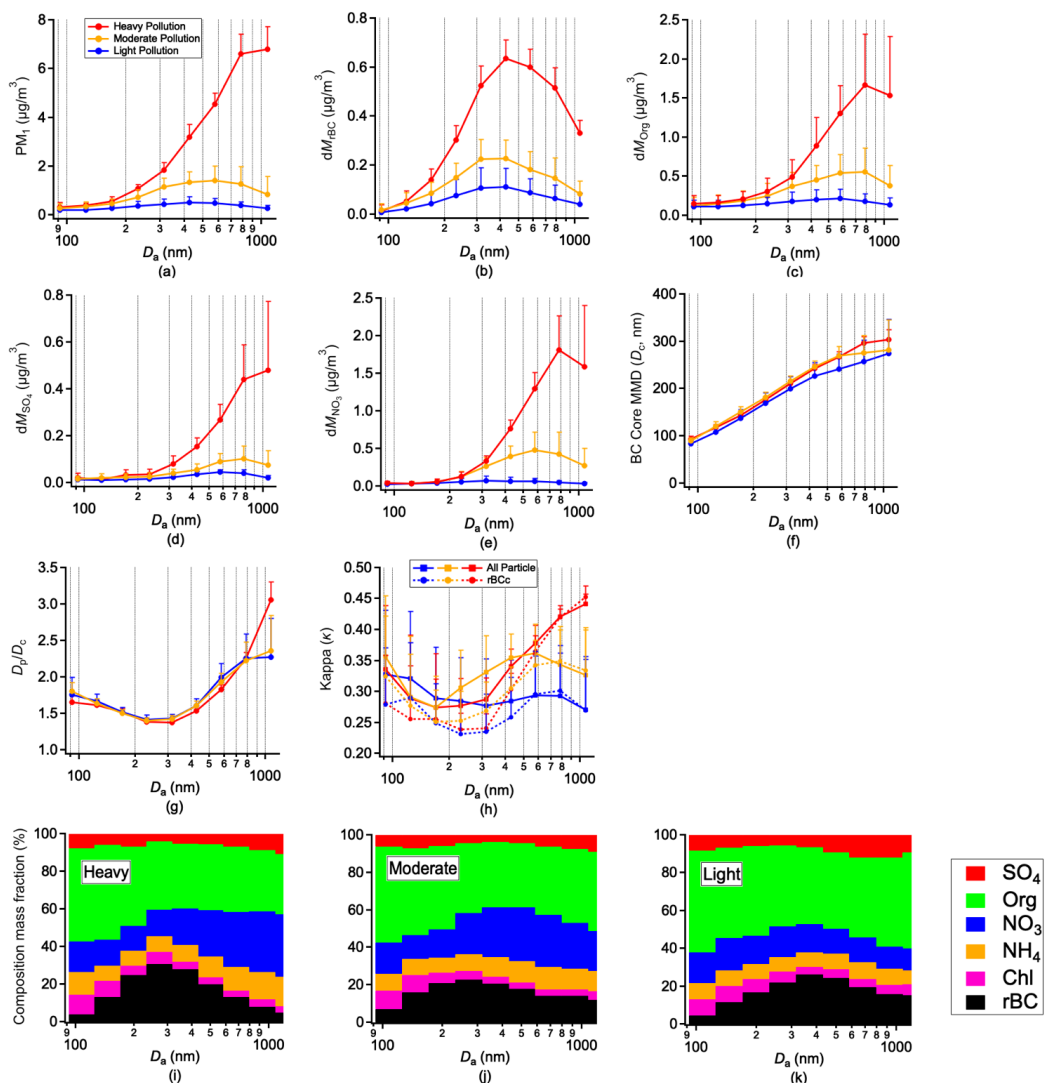
898

899 Figure 3 An example of the calculation of the size-resolved critical supersaturation
900 (SSc)

901



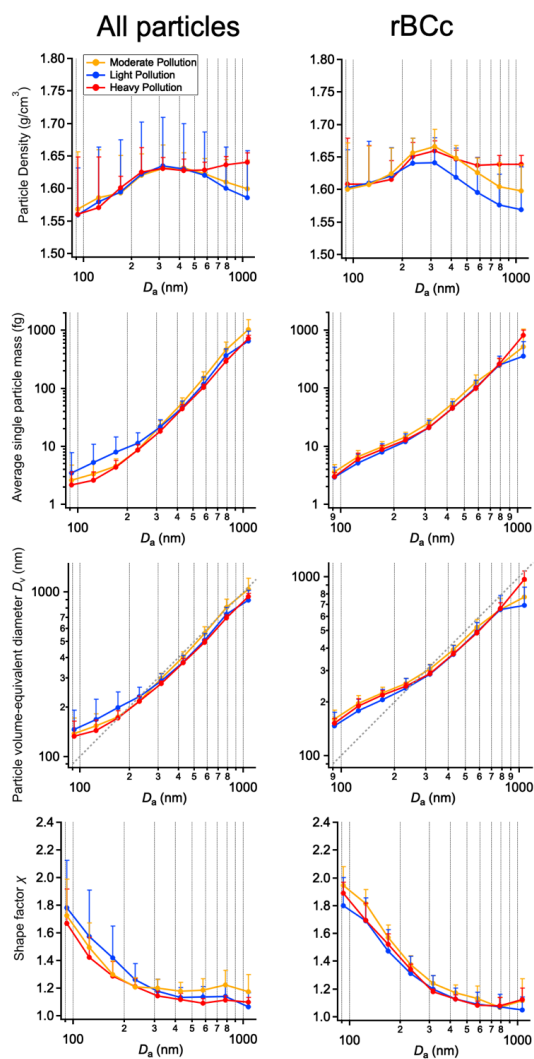
904 Figure 4. Overview of the experiment. (a) Location of the measurement site (marked in
905 red pentagram) and regions classified for air mass; (b) The mean aerosol optical depth
906 (AOD) distribution during the experiment period; (c) Aerosol mass and number
907 concentrations and classified air mass types.



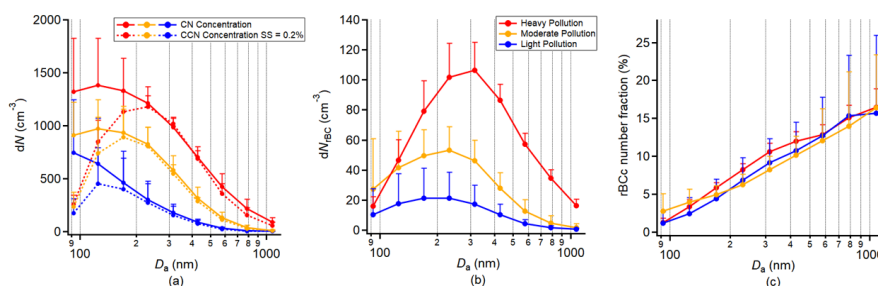
908

909 Figure 5 Size-resolved (a) PM_{10} (mean \pm standard deviation); (b) rBC mass
 910 concentration; (c) Org mass concentration; (d) SO_4 mass concentration; (e) NO_3 mass
 911 concentration; (f) size-resolved rBC core mass median diameter (MMD); (g) size-
 912 resolved coating thickness (D_p/D_c) of rBCc; (h) hygroscopicity parameter (κ); (i, j, k)
 913 aerosol composition mass fractions under three different pollution levels.

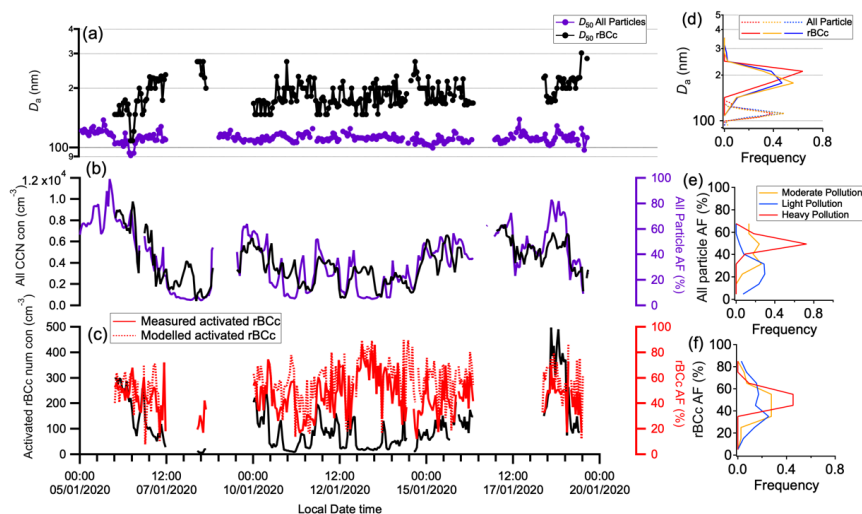
914



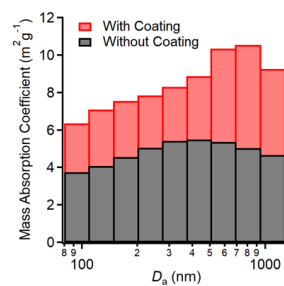
915
916 Figure 6 The particle density, average single particle mass, shape factor and volume-
917 equivalent diameter for all particles (All Particles, left) and refractory Black Carbon
918 containing particles (rBCc, right) under different pollution level.
919



920
 921 Figure 7 Size-resolved (a) CN and CCN at SS = 0.2% number concentrations; (b) rBC
 922 number concentration; (c) rBCc number fraction.
 923



924
 925 Figure 8 CCN activities of all particles and rBCc. (a) Time series of D_{50} for all particles
 926 and rBCc; (b) Time series of all CCN number concentrations and all particles activation
 927 fractions; (c) Time series of measured activated rBCc number concentrations, and rBCc
 928 activation fractions from two methods; (d) Frequency of D_{50} for all particle and rBCc;
 929 (e) Frequency of all particles activation fraction; (f) Frequency of measured rBCc
 930 activation fraction.
 931



932

933 Figure 9 Mass Absorption Coefficient (MAC) at 880 nm wavelength for coated and
934 uncoated rBCs.

935